

PAPER

Thermoelectric properties of $\text{Co}_4\text{Sb}_{12}$ with Bi_2Te_3 nano-inclusions

To cite this article: Sanyukta Ghosh *et al* 2018 *J. Phys.: Condens. Matter* **30** 095701

View the [article online](#) for updates and enhancements.

Related content

- [Odyssey of thermoelectric materials: foundation of the complex structure](#)
Khalid Bin Masood, Pushpendra Kumar, R A Singh *et al.*
- [Thermoelectric properties of Bi-added \$\text{Co}_4\text{Sb}_{12}\$ skutterudites](#)
R C Mallik, R Anbalagan, K K Raut *et al.*
- [Enhanced thermoelectric performance of \$\text{Bi}_2\text{Te}_3\$ through uniform dispersion of single wall carbon nanotubes](#)
Kaleem Ahmad and Chunlei Wan

Recent citations

- [Nanostructuring as a tool to adjust thermal expansion in high ZT skutterudites](#)
G. Rogl *et al*



IOP | ebooks™

Bringing together innovative digital publishing with leading authors from the global scientific community.

Start exploring the collection—download the first chapter of every title for free.

Thermoelectric properties of $\text{Co}_4\text{Sb}_{12}$ with Bi_2Te_3 nano-inclusions

Sanyukta Ghosh¹, Anuj Bisht², Anirudha Karati³, Gerda Rogl^{4,5},
Peter Rogl^{4,5}, B S Murty⁶, Satyam Suwas² and Ramesh Chandra Mallik¹ 

¹ Thermoelectric Materials and Devices Laboratory, Department of Physics, Indian Institute of Science, Bangalore 560012, India

² Department of Materials Engineering, Indian Institute of Science, Bangalore 560012, India

³ Department of Chemistry, Indian Institute of Technology, Madras, Chennai-600036, India

⁴ Institute of Materials Chemistry and Research, University of Vienna, Währingerstrasse 42, Wien, Austria

⁵ Christian Doppler Laboratory for Thermoelectricity, Wien, Austria

⁶ Department of Metallurgical and Materials Engineering, Indian Institute of Technology, Madras, Chennai-600036, India

E-mail: rcmallik@iisc.ac.in

Received 23 November 2017, revised 16 December 2017

Accepted for publication 8 January 2018

Published 12 February 2018



Abstract

The figure of merit (zT) of a thermoelectric material can be enhanced by incorporation of nano-inclusions into bulk material. The presence of bismuth telluride (Bi_2Te_3) nano-inclusions in $\text{Co}_4\text{Sb}_{12}$ leads to lower phonon thermal conductivity by introducing interfaces and defects; it enhances the average zT between 300–700 K. In the current study, Bi_2Te_3 nanoparticles were dispersed into bulk $\text{Co}_4\text{Sb}_{12}$ by ball-milling. The bulk was fabricated by spark plasma sintering. The presence of Bi_2Te_3 dispersion in $\text{Co}_4\text{Sb}_{12}$ was confirmed by x-ray diffraction, scanning electron microscopy, transmission electron microscopy and electron back scattered diffraction technique. Energy dispersive spectroscopy showed antimony (Sb) as an impurity phase for higher contents of Bi_2Te_3 in the sample. The Seebeck coefficient (S) and electrical conductivity (σ) were measured in the temperature range of 350–673 K. The negative value of S indicates that most of the charge carriers were electrons. A decrease in S and increase in σ with Bi_2Te_3 content are due to the increased carrier concentration, as confirmed by Hall measurement. The thermal conductivity, measured between 423–673 K, decreased due to the increased phonon scattering at interfaces. A maximum zT of 0.17 was achieved at 523 K and it did not vary much throughout the temperature range. The experimental results of composites were compared by using effective medium theories.

Keywords: thermoelectric materials, skutterudite, bismuth telluride, nanocomposites

(Some figures may appear in colour only in the online journal)

1. Introduction

Thermoelectricity is one of the simplest energy conversion technologies, in which electricity is generated when a temperature gradient is introduced. It has attracted remarkable attention because of its application in power generation and solid-state cooling with the benefits of small size, less weight, long life, high reliability, no moving parts, fast response and

no pollutants. The efficiency of this conversion depends on the performance of the thermoelectric material, which is defined by the dimensionless figure of merit $zT = S^2\sigma T/\kappa$, where T is the temperature and κ is the thermal conductivity. To achieve an efficiency comparable to commercially available energy conversion devices, zT of 3 is required. The maximum reported zT is 2.6 for a tin selenide (SnSe) single crystal [1]. Currently, researchers are adopting various approaches to maximize zT

either by maximizing the power factor ($S^2\sigma$) or reducing κ as much as possible.

Skutterudite based thermoelectric materials are considered as one of the most efficient materials for mid-temperature thermoelectric generator applications. Binary skutterudites with the chemical formula MA_3 ($M = \text{Co, Ir, Rh}$ and $A = \text{P, As, Sb}$) have shown interesting thermoelectric properties at mid temperature ranges (400–700 K). The unit cell has been identified as a body-centred cubic structure with space group $Im\bar{3}$ having eight formula units, 32 atoms and two voids per unit cell. It satisfies most of the requirements of a good thermoelectric material such as highly symmetric crystal structure, large unit cell, high average atomic mass, high carrier mobility, covalent bond between constituent atoms, high Seebeck coefficient and moderate electrical conductivity. However it has a high lattice thermal conductivity (κ_l) compared to other thermoelectric materials ($7.5 \text{ W m}^{-1} \text{ K}^{-1}$ at 300 K for $\text{Co}_4\text{Sb}_{12}$), which results in low zT [2] and low device efficiency. The effective way to enhance zT is to reduce κ_l without effecting the interrelated S , σ and electronic thermal conductivity (κ_e). Several approaches have been taken to decrease κ_l of bulk $\text{Co}_4\text{Sb}_{12}$ such as (i) incorporation of guest atoms into the two voids in the structure [3–7], (ii) substitution of the parent atoms, Co and Sb, by foreign atoms [8–12] and (iii) introduction of nanoparticles into the matrix to form nanocomposites.

Nanocomposites comprise two or more immiscible phases having different properties, wherein at least one phase is restricted to the nanometer order. In recent years, nanocomposites are being regarded as a promising solution to reduce the lattice thermal conductivity. Introducing a secondary phase into the bulk material enhances the grain boundary density and the number of interfaces, which act as effective scattering centres for phonons. Nano-inclusions may also lead to impurity defects that result in a further decrease in κ_l . Some theoretical studies have been carried out to investigate the effects of shape and size of the inclusions and the microstructure on transport properties of the composite [13, 14]. In the case of homogeneous dispersion of nanoparticles into the matrix, a significant reduction in κ_l is possible due to the strong scattering of mid-long wavelength phonons with less effect on short wavelength electrons. The transport of charge carriers is also influenced by the distribution of the secondary phases in the nanocomposite. Electrons may be scattered at interfaces, which leads to low electron mobility and low electrical conductivity. It is very challenging to separate the scattering of phonons and electrons at interfaces. Furthermore, if the Fermi levels of the matrix phase and dispersion are different, electron transfer will take place from the phase having a higher Fermi level to the lower one. Therefore, the band will bend away from the interface and will develop a potential barrier [15–17]. To enhance thermopower, it may be useful to filter the low energy carriers and increase the carrier density of states near the Fermi level. A low work function of inclusions is also required for an electron transfer between two phases. If the inclusion is more electrically conducting than the matrix, the Fermi level of the dispersion will be higher than that of the matrix. This way electron transfer will take place from the inclusion to the matrix, which will result in a higher electrical

conductivity in the composite due to increased carrier concentration. Conversely, using an insulator as an inclusion is more effective to lower the thermal conductivity, but composites have some limitations. Bergman *et al* [18, 19] showed (from calculations) that zT of a binary composite material cannot exceed the highest zT of the individual components. The effective medium approximation [20, 21] also predicts that the value of electrical conductivity and thermal conductivity of composites will be an average of the two phases without considering the effects of interfaces and grain boundaries. Some experiments have even shown a decrease of zT in nanocomposites [22]. But recently, some works on composites [23] have reported that zT of composites can be enhanced by optimizing the inclusion size and microstructures which enhance the phonon scattering and reduce the lattice thermal conductivity effectively. Furthermore, the energy filtering effect at the interfaces enhances the Seebeck coefficient and consequently, the power factor.

Recently, many studies have reported on the effect of dispersions on the thermoelectric properties of bulk $\text{Co}_4\text{Sb}_{12}$ [23–35]. An enhancement in zT has been observed through the addition of nanoparticles, which greatly decreased thermal conductivity compared to the bulk. Shi *et al* [23] reported that κ_l of $\text{Co}_4\text{Sb}_{12}$ and fullerene (C_{60}) composites reduced dramatically compared to the matrix, and a zT value of 1.3 was achieved with an appropriate quantity of dispersants. Zhou *et al* [24] have noted large improvements in both electrical conductivity and Seebeck coefficient as well as a large reduction in thermal conductivity in $\text{Ag}/\text{Ba}_{0.3}\text{Co}_4\text{Sb}_{12}$ nanocomposites, which produced an enhanced zT value of 1.0 at 823 K. In addition, nanocomposites such as $\text{Co}_4\text{Sb}_{12}/\text{ZrO}_2$ [25], $\text{Co}_4\text{Sb}_{12}/\text{graphene}$ [26], $\text{Co}_4\text{Sb}_{12}/\text{WO}_3$ [27], $\text{Co}_4\text{Sb}_{12}/\text{PbTe}$ [28], $\text{Co}_4\text{Sb}_{11.7}\text{Te}_{0.3}/\text{TiO}_2$ [29] and $\text{CoSb}_3/\text{WTe}_2$ [30] showed significant decrease in thermal conductivity providing a great enhancement in zT . Specifically, $\text{Yb}_y\text{Co}_4\text{Sb}_{12}/\text{Yb}_2\text{O}_3$ composites have shown a remarkable decrease in thermal conductivity leading to a high zT of 1.38 at 850 K [31]. Yb_2O_3 as a homogeneous nanoscale distribution in $(\text{Sr}_{0.25}\text{Ba}_{0.25}\text{Yb}_{0.50})_{0.5}\text{Co}_4\text{Sb}_{12.5}$ improved the thermoelectric performance, resulting in a zT value of 1.6 at 835 K [32]. According to another report, ultra-low thermal conductivity with an enhanced Seebeck coefficient was obtained from gallium antimonide (GaSb) dispersed $\text{Yb}_{0.26}\text{Co}_4\text{Sb}_{12}$ nanocomposite materials, with an improved zT of 1.45 at 850 K [33]. Recently, Moure *et al* [34] have reported zT values close to 1.0 in $\text{CoSb}_3/\text{oxide}$ nanocomposites due to the effective decoupling of thermal and electrical properties.

In the present work, nanocomposites made of randomly dispersed Bi_2Te_3 in the host matrix of bulk $\text{Co}_4\text{Sb}_{12}$ were synthesized. The influence of Bi_2Te_3 nanoparticles on the thermoelectric properties of bulk $\text{Co}_4\text{Sb}_{12}$ was investigated for a wide temperature range. The reason for using Bi_2Te_3 is that it has high electrical conductivity that can compensate for the power factor degradation at interfaces. In addition, Bi_2Te_3 has the highest zT of 0.6 at 300 K [36] and $\text{Co}_4\text{Sb}_{12}$ has the highest zT of 0.08 at 623 K [2]. Thus, the Bi_2Te_3 -added $\text{Co}_4\text{Sb}_{12}$ composite material was expected to have a high average zT between 300–700 K and a low lattice thermal conductivity due to increased grain boundaries and interfaces. A significant enhancement in

the power factor and remarkable decrease in thermal conductivity resulted in improved zT values. A maximum zT of 0.17 was obtained at 523 K and the average zT improved for the whole temperature range. The experimental electrical conductivity and thermal conductivity of the composites were examined in the context of the effective medium theory proposed by Lewis and Nielson. The experimental Seebeck coefficient was compared with the theoretical Webman–Jortner–Cohen (WJC) model [37].

2. Experimental procedure

2.1. Synthesis

Highly pure cobalt (99.995%) and antimony (99.999%) were weighed according to stoichiometric ratio and sealed under dynamic vacuum (5×10^{-2} Pa) in quartz ampoules. The material was induction-melted for 10 min at 1130 K followed by rapid quenching in water. The sample was annealed at 973 K for 168 h. The ingot was hand-ground into powder by using a mortar and pestle and then ball-milled at 250 rpm for 6 h. The Bi_2Te_3 powder was mixed with $\text{Co}_4\text{Sb}_{12}$ powder according to the chemical formula $(\text{Bi}_2\text{Te}_3)_x\text{Co}_4\text{Sb}_{12}$ (where $x = 0.1, 0.2, 0.3, 0.4$) and the mixed material was ball-milled at 250 rpm for 1 h. The composite powder was compacted by spark plasma sintering using Dr. Sinter SPS-625 at 823 K for 5 min with 50 MPa pressure under 0.5 mbar vacuum. All the samples were cut into rectangular pellets ($10 \times 2 \times 2 \text{ mm}^3$) to measure the electrical conductivity and Seebeck coefficient and a circular pellet (6 mm diameter \times 1 mm thickness) to measure the thermal conductivity.

2.2. Characterization

Powder x-ray diffraction (XRD) was carried out by the Rigaku Smartlab diffraction system using Cu K_α radiation with a step size of 0.02° and 2θ range $5\text{--}90^\circ$ for phase identification of the samples. High temperature XRD was done by XPERTPro, PANalytical from room temperature to 723 K. The surface morphology of the sample was observed by scanning electron microscopy (SEM) using FEI ESEM Quanta 200 and the composition of the sample was detected by energy dispersive spectroscopy (EDS) using an electron probe micro analyzer (EPMA), namely JEOL JXA-8530F. Electron back scattered diffraction (EBSD) was performed to capture the microstructural details of the composites. EBSD was carried out at an accelerating voltage of 25 kV by scanning a sample area of $2 \mu\text{m} \times 4 \mu\text{m}$ with a step size of 20 nm using FEI Helios NanoLab Dualbeam. The grain boundaries and interfaces in the composite were studied by high resolution transmission electron microscopy (HRTEM) using a FEI Tecnai F-30 with a field emission source operated at 300 kV. To prepare samples for TEM, powder samples were suspended in ethanol and drop-cast on carbon-coated copper grids. The grids were dried using infrared radiation. The carrier concentration of the samples was measured by the Hall method at room temperature under a magnetic field of 0.25 T. The density of the samples was measured using Archimedes' principle. The Seebeck coefficient (S) and electrical resistivity (ρ) were measured by

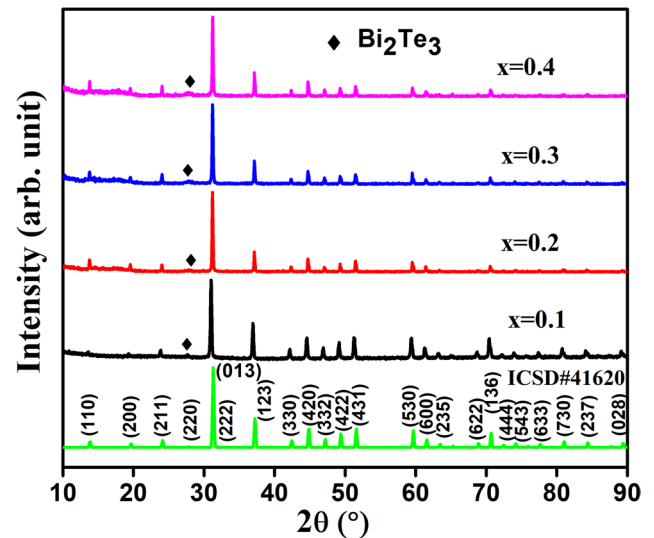


Figure 1. Powder XRD patterns of $(\text{Bi}_2\text{Te}_3)_x\text{Co}_4\text{Sb}_{12}$ ($x = 0.1, 0.2, 0.3, 0.4$).

the differential method and four probe method respectively using a Linseis LSR-3 from room temperature to 673 K. The laser flash method was used to determine thermal conductivity ($\kappa = DC_p d$) of the samples from 423–673 K using a Flashline 3000 (ANTER), where D is the diffusivity of the sample, C_p is the specific heat and d is the density.

3. Results and discussions

3.1. Structural characterization

The powder and compacted pellet were investigated using XRD for structural phase determination. Figure 1 shows the XRD pattern of $(\text{Bi}_2\text{Te}_3)_x\text{Co}_4\text{Sb}_{12}$ (where $x = 0.1, 0.2, 0.3, 0.4$) annealed and sintered composites. All the peaks were identified as δ -phase $\text{Co}_4\text{Sb}_{12}$ with $Im\bar{3}$ symmetry and indexed with the relevant Miller indices (ICSD#41620). The highest peak of Bi_2Te_3 is at $2\theta = 27.7^\circ$ [38] which was overlapping with the peak of the matrix phase. The peaks corresponding to the Bi_2Te_3 phase were not properly resolvable from the matrix phase as the amount of inclusion in the composite was very small. Another possible reason may be the very small grain size of the nano- Bi_2Te_3 particles that cannot generate sharp diffraction peaks. The Rietveld refinement was used to refine the structural parameters considering a pseudo-Voigt profile function with no preferred crystal orientation. A quantitative Rietveld analysis was done considering inclusion as the secondary phase, which improved the quality of the Rietveld refinement. A Rietveld analysis of the XRD pattern of $(\text{Bi}_2\text{Te}_3)_{0.2}\text{Co}_4\text{Sb}_{12}$ at room temperature is shown in figure 2. A Rietveld analysis of the powder XRD pattern confirmed the presence of $\text{Co}_4\text{Sb}_{12}$ with a small amount of Bi_2Te_3 as secondary phase that increased with increasing amounts of Bi_2Te_3 . No peak shifts were observed with increasing Bi_2Te_3 content; this indicates that Bi_2Te_3 had not occupied the void (2a sites) but formed a secondary phase as expected for a composite sample. This conclusion was also confirmed by calculating the lattice parameters (a) of all samples using Rietveld

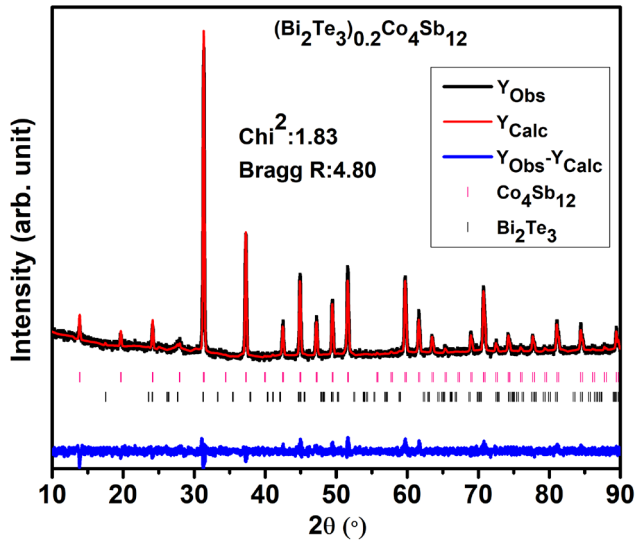


Figure 2. Rietveld refinement analysis of powder XRD pattern of $(\text{Bi}_2\text{Te}_3)_{0.2}\text{Co}_4\text{Sb}_{12}$.

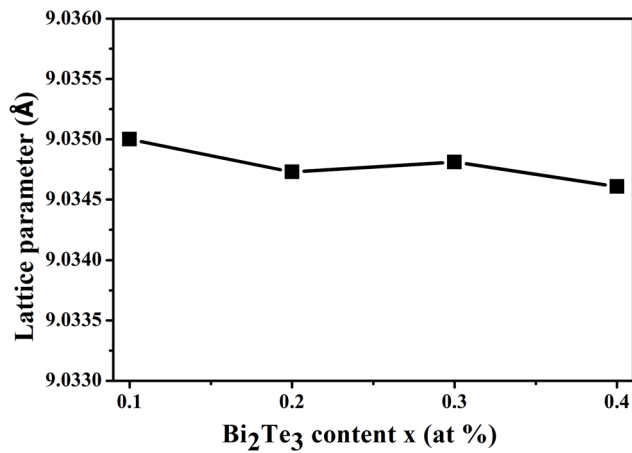


Figure 3. Lattice parameter of the as-synthesized $(\text{Bi}_2\text{Te}_3)_x\text{Co}_4\text{Sb}_{12}$ nanocomposite as a function of Bi_2Te_3 content.

refinement. There was no change in a at room temperature as a function of Bi_2Te_3 content (figure 3).

No structural change was observed in high temperature XRD except a shift of peaks. At high temperature, atoms gain extra kinetic energy from the heat energy and start to vibrate and repel each other. Therefore, the unit cell expands with temperature because of the increased separation between atoms, which causes the expansion of lattice parameters and volume of the unit cell as shown in figure 4. The linear thermal expansion coefficient (α_a) and volume thermal expansion coefficient (α_v) were calculated by using the equations: $\alpha_a = \frac{1}{a} \frac{da}{dT}$ and $\alpha_v = \frac{1}{v} \frac{dv}{dT}$ where v is the volume of the unit cell ($v = a^3$) and $\frac{da}{dT}$ and $\frac{dv}{dT}$ are the rate of change of the lattice parameter and volume respectively with temperature. Figure 5 shows that α_a and α_v decrease with temperature which results in lower thermal stress at elevated temperatures.

Figures 6(a)–(d) show the SEM backscattered micrographs of $(\text{Bi}_2\text{Te}_3)_x\text{Co}_4\text{Sb}_{12}$ (where $x = 0.1, 0.2, 0.3, 0.4$). The surface of the samples showed the presence of very small pores; this suggests good densification, which is in good agreement

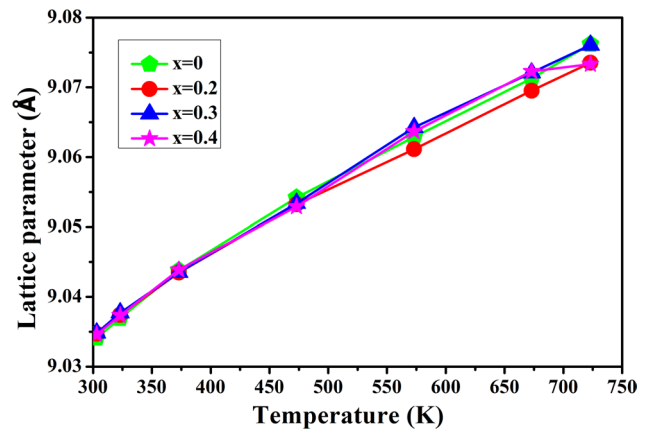


Figure 4. Temperature dependence of lattice parameter of $(\text{Bi}_2\text{Te}_3)_x\text{Co}_4\text{Sb}_{12}$ ($x = 0, 0.2, 0.3, 0.4$).

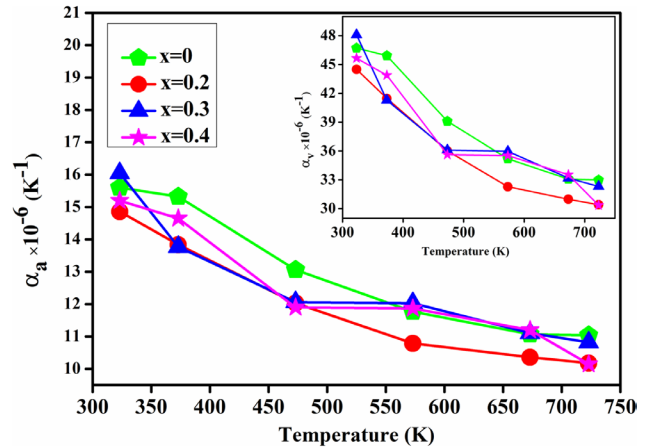


Figure 5. Linear thermal expansion coefficient as a function of temperature, inset: temperature dependence of volume thermal expansion coefficient.

with the density of the samples obtained using Archimedes' principle (97% of the theoretical density). Similar morphologies were observed for all the samples. The light grey area in figures 6(a)–(d) is the $\text{Co}_4\text{Sb}_{12}$ phase and white area is the Bi_2Te_3 phase. The irregularly shaped Bi_2Te_3 nanoparticles were randomly distributed in the $\text{Co}_4\text{Sb}_{12}$ matrix. A small amount of elemental Sb (dark grey area) phase was also observed for $x \geq 0.2$, but no corresponding peak for Sb was observed in the XRD pattern. The average compositions of different phases detected by EDS in EPMA mode are listed in table 1. In EDS, the presence of Sb in the Bi_2Te_3 phase was observed. Composition was not detected properly in EDS as the L_α energy of Te (3.769 eV) and Sb (3.604 eV) are very close. The carrier concentration at room temperature, as detected by the Hall measurement, increased with increasing Bi_2Te_3 content; this is listed in table 1.

Figures 7(a) and (b) show the EBSD generated phase map of $(\text{Bi}_2\text{Te}_3)_x\text{Co}_4\text{Sb}_{12}$ composites with $x = 0.2$ and 0.4 . In the phase map, the green color represents the $\text{Co}_4\text{Sb}_{12}$ phase and red and yellow color represent Bi_2Te_3 and the Sb phase, respectively. Micrographs showed two types of regions: Bi_2Te_3 and Sb phases were distributed at the grain boundary of the $\text{Co}_4\text{Sb}_{12}$ phase in one region. In the other region, randomly

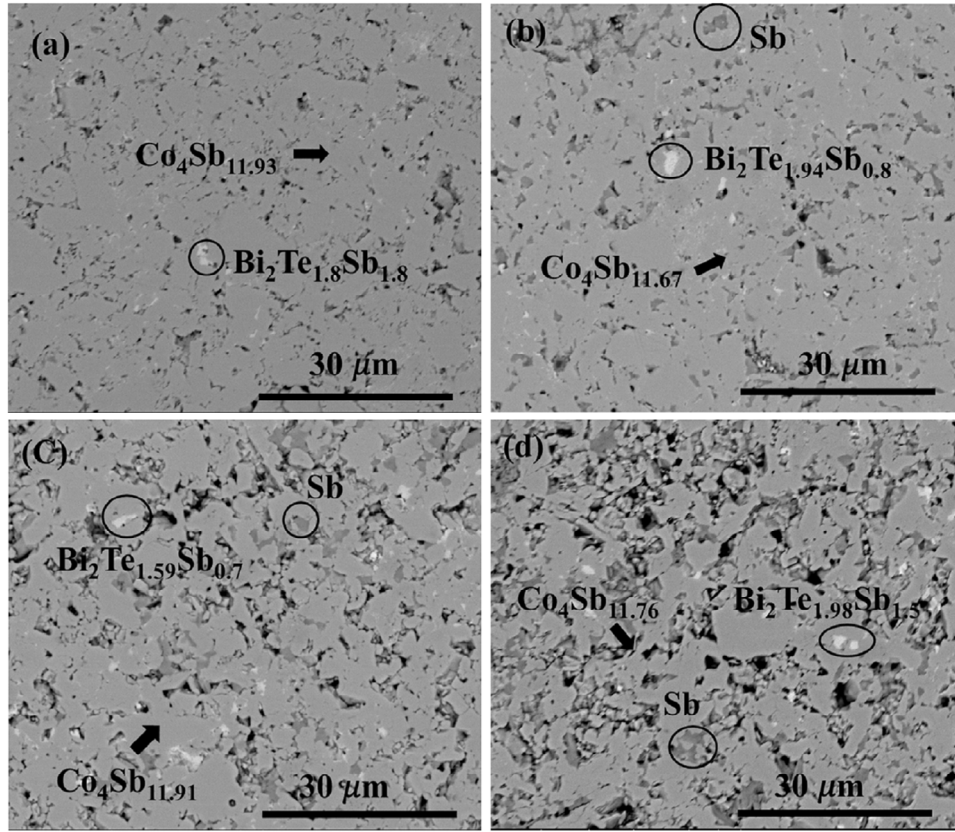


Figure 6. SEM micrographs of (a) $(\text{Bi}_2\text{Te}_3)_{0.1}\text{Co}_4\text{Sb}_{12}$, (b) $(\text{Bi}_2\text{Te}_3)_{0.2}\text{Co}_4\text{Sb}_{12}$, (c) $(\text{Bi}_2\text{Te}_3)_{0.3}\text{Co}_4\text{Sb}_{12}$, (d) $(\text{Bi}_2\text{Te}_3)_{0.4}\text{Co}_4\text{Sb}_{12}$.

Table 1. Composition determined by EDS, band gap and carrier concentration at room temperature (300 K) of $(\text{Bi}_2\text{Te}_3)_x\text{Co}_4\text{Sb}_{12}$ nanocomposite.

Sample	Composition			Bandgap $E_g = (2IS_{\max}/T_{\max})$ in eV	Carrier concentration at room temperature /cm ³
	Light grey region ($\text{Co}_4\text{Sb}_{12}$)	White region (Bi_2Te_3)	Dark grey region (Sb)		
$x = 0.1$	$\text{Co}_4\text{Sb}_{11.93}(\text{Bi}_{0.003})$	$\text{Bi}_2\text{Te}_{1.8}(\text{Co}_{0.41}\text{Sb}_{1.8})$	—	0.19	6.70×10^{19}
$x = 0.2$	$\text{Co}_4\text{Sb}_{11.67}(\text{Bi}_{0.003})$	$\text{Bi}_2\text{Te}_{1.94}(\text{Co}_{0.2}\text{Sb}_{0.8})$	$\text{Sb}_{0.95}(\text{Bi}_{0.003}\text{Te}_{0.002}\text{Co}_{0.03})$	0.17	8.47×10^{19}
$x = 0.3$	$\text{Co}_4\text{Sb}_{11.91}(\text{Bi}_{0.003})$	$\text{Bi}_2\text{Te}_{1.59}(\text{Co}_{0.2}\text{Sb}_{0.7})$	$\text{Sb}_{0.9}(\text{Bi}_{0.005}\text{Te}_{0.007}\text{Co}_{0.08})$	0.15	1.25×10^{20}
$x = 0.4$	$\text{Co}_4\text{Sb}_{11.76}(\text{Bi}_{0.002})$	$\text{Bi}_2\text{Te}_{1.98}(\text{Co}_{0.3}\text{Sb}_{1.5})$	$\text{Sb}_{0.88}(\text{Bi}_{0.001}\text{Te}_{0.015}\text{Co}_{0.1})$	0.15	1.42×10^{20}

dispersed Bi_2Te_3 phase and Sb impurity phase were observed within the parent $\text{Co}_4\text{Sb}_{12}$ grain. The effective grain size of the two regions was different. The average grain size of pure $\text{Co}_4\text{Sb}_{12}$ was around $1 \mu\text{m}$. The grain size of Bi_2Te_3 inclusion was in the order of a few nm. The first region was prominent in the composite with $x = 0.2$, whereas the second region was prominent in the composite with $x = 0.4$ because of the comparatively large amount of Bi_2Te_3 .

The HRTEM of two samples shows that the composites have high grain density with sharp grain boundaries, as shown in figures 8(a)–(d). The region (second region mentioned in EBSD micrographs) where Bi_2Te_3 and Sb phases were agglomerated inside the parent grain of $\text{Co}_4\text{Sb}_{12}$ was investigated by TEM. Due to the small size (few nm) of phases in the composite, it was difficult to determine the grain size from the HRTEM micrographs of the agglomerate as it often contained overlapped grains. Three different phases were observed in the HRTEM micrograph, which agrees with the SEM, EPMA and

EBSD results. A fast Fourier transform (FFT) generated from one phase showed cubic symmetry, indicating the presence of $\text{Co}_4\text{Sb}_{12}$ (figures 8(b) and (d)). The FFT generated from other regions showed hexagonal symmetry, which stems from Bi_2Te_3 and Sb phases. Figure 8(b) shows that the $\text{Co}_4\text{Sb}_{12}$ particle aligned along the $[001]$ direction is parallel to the beam direction. The interplanar spacing of lattice fringes of $\text{Co}_4\text{Sb}_{12}$ was 0.320 nm , which corresponds to the (220) plane. Figure 8(d) shows a fringe spacing of 0.322 nm corresponding to the (300) plane of $\text{Co}_4\text{Sb}_{12}$.

3.2. Transport properties

Figure 9 shows the variation of electrical conductivity with temperature. σ decreased with increasing temperature up to about 450 K and thereafter increased due to the generation of more charge carriers at high temperatures, indicating the semiconducting behaviour of composites. Another reason for

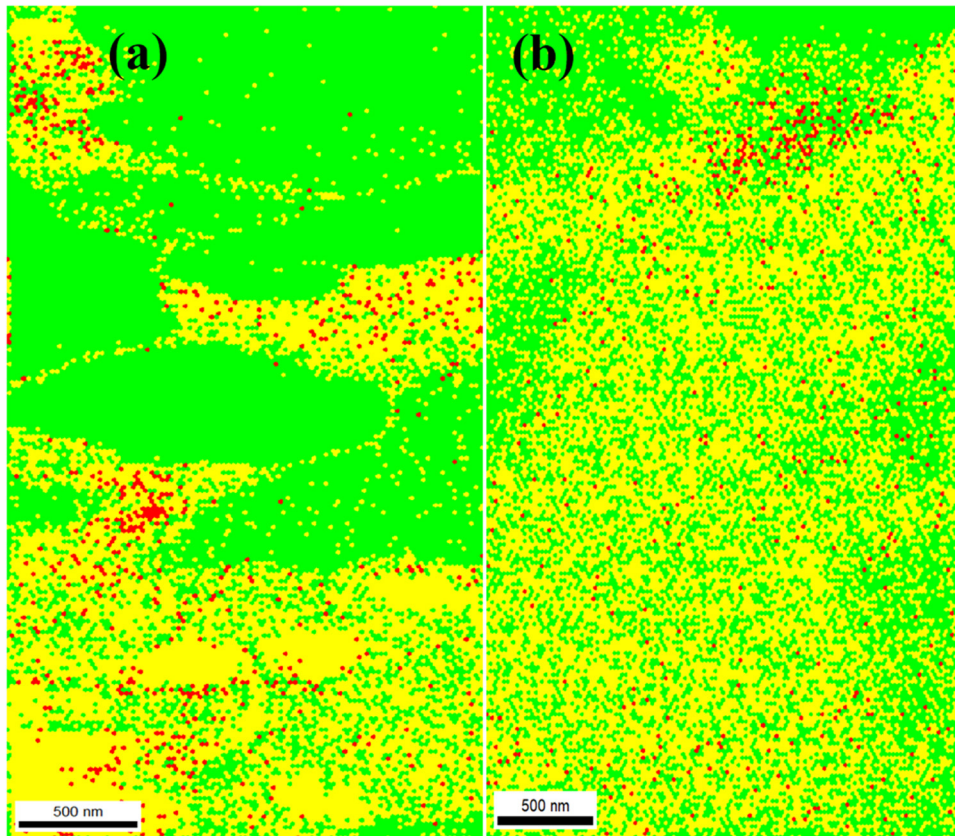


Figure 7. EBSD phase maps of (a) $(\text{Bi}_2\text{Te}_3)_{0.2}\text{Co}_4\text{Sb}_{12}$, (b) $(\text{Bi}_2\text{Te}_3)_{0.4}\text{Co}_4\text{Sb}_{12}$.

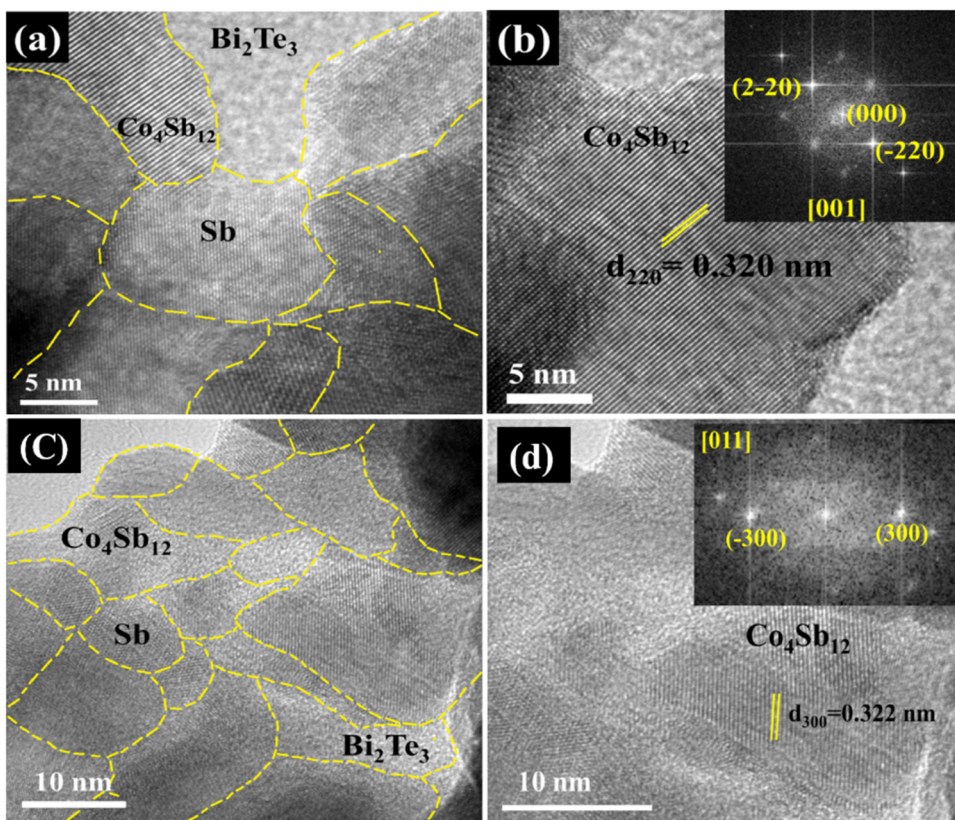


Figure 8. (a) High resolution TEM micrograph of $(\text{Bi}_2\text{Te}_3)_{0.2}\text{Co}_4\text{Sb}_{12}$ showing high density of grains with sharp grain boundaries, (b) FFT of crystalline phase $\text{Co}_4\text{Sb}_{12}$, (c) and (d) high resolution TEM micrographs obtained from $(\text{Bi}_2\text{Te}_3)_{0.4}\text{Co}_4\text{Sb}_{12}$ in similar fashion.

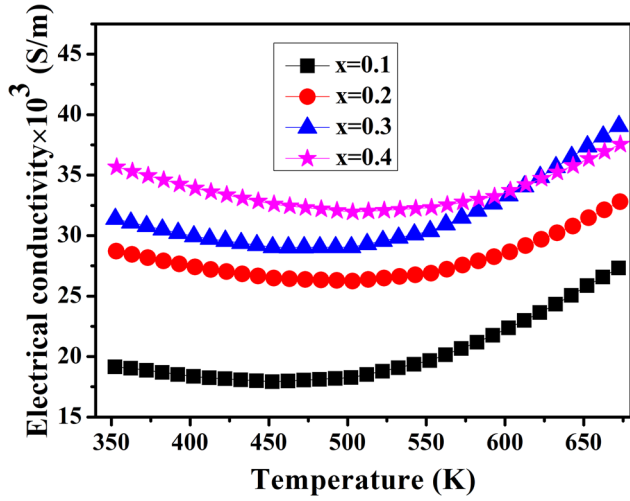


Figure 9. Temperature dependence of electrical conductivity of $(\text{Bi}_2\text{Te}_3)_x\text{Co}_4\text{Sb}_{12}$ ($x = 0.1, 0.2, 0.3, 0.4$).

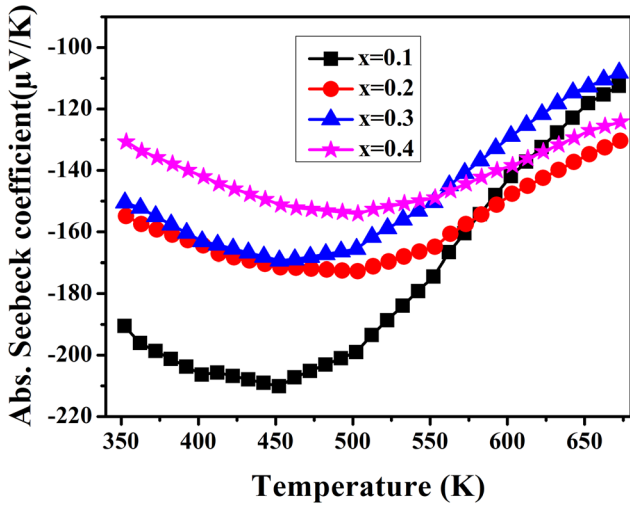


Figure 10. Temperature dependence of Seebeck coefficient of $(\text{Bi}_2\text{Te}_3)_x\text{Co}_4\text{Sb}_{12}$ ($x = 0.1, 0.2, 0.3, 0.4$).

the higher value of electrical conductivity at high temperatures is bipolar conduction. The minority charge carriers (holes) also become effective at this temperature range and take part in conduction. The electrical conductivity (σ) in the case of bipolar conduction can be expressed as: $\sigma = n_e e \mu_e + n_p p \mu_p$, where n_e and n_p are the concentration of electrons and holes respectively, μ_e and μ_p are the mobility of electrons and holes respectively. With increasing Bi_2Te_3 content, σ increased greatly compared to bulk $\text{Co}_4\text{Sb}_{12}$ as Bi_2Te_3 contributes electrons to the system as confirmed by the Hall measurement data (table 1). The presence of a highly conductive Sb impurity phase in the composite with $x \geq 0.2$ is also responsible for high σ .

The temperature dependence of the Seebeck coefficient (S) is shown in figure 10. S was positive for pristine $\text{Co}_4\text{Sb}_{12}$ suggesting that it is a p type conductor. On the other hand, S was negative for pristine Bi_2Te_3 indicating its n-type semiconducting nature. As a result of this, S changed to negative for all the composite samples indicating that the majority of charge carriers were electrons. It was due to the electron transfer

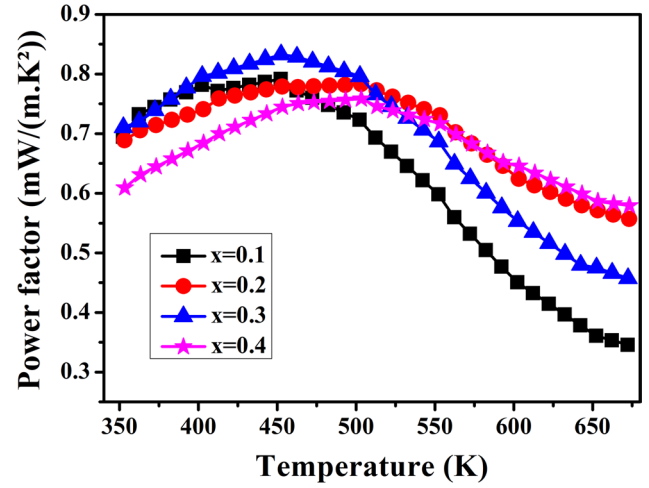


Figure 11. Temperature dependence of power factor of $(\text{Bi}_2\text{Te}_3)_x\text{Co}_4\text{Sb}_{12}$ ($x = 0.1, 0.2, 0.3, 0.4$).

from the Bi_2Te_3 phase to the matrix phase. S decreased with the addition of Bi_2Te_3 content at room temperature. According to the Pisarenko relation, S is inversely proportional to $2/3$ of the carrier concentration [39]. Therefore, the decrease in S is due to the increased electron concentration provided by Bi_2Te_3 to the matrix. Moreover, S also showed the same transition as electrical conductivity around 450 K: S increased with temperature and reached a maximum value at about 450 K and then started to decrease at higher temperatures. The decrease in S may be due to bipolar conduction. When two types of charge carriers are present in the system, S is given by [28, 40, 41]:

$$S = \frac{S_n \sigma_n + S_p \sigma_p}{\sigma_n + \sigma_p} \quad (1)$$

where S_n is the Seebeck coefficient due to electrons, S_p is the Seebeck coefficient due to holes, σ_n and σ_p are the electrical conductivities of electrons and holes respectively. Though the majority of charge carriers were electrons, the contribution from holes suppressed S effectively at high temperatures because of the higher mobility of holes. The band gap of the composites was calculated from the maximum S value (S_{\max}) and the corresponding temperature T_{\max} by using the equation $E_g = 2e |S_{\max}| T_{\max}$ proposed by Goldsmid and Sharp [40]. The band gap of $\text{Co}_4\text{Sb}_{12}$ is 0.22 eV [42] and the band gap of Bi_2Te_3 is 0.16 eV [43]. The estimated band gap (reported in table 1) of the nanocomposite decreased with increasing Bi_2Te_3 content compared to matrix $\text{Co}_4\text{Sb}_{12}$; this can be attributed to the increased carrier concentration of the nanocomposite. The carrier concentration is related to the band gap via the relation: $n = A \exp(-E_g/2k_B T)$ where A is a pseudo constant, E_g is the band gap, k_B is Boltzmann's constant and T is the temperature. Therefore, the decrease of the band gap in the nanocomposite is due to the increase in carrier concentration.

Figure 11 shows the temperature dependency of the power factor. A maximum power factor of $0.83 \text{ mW m}^{-1} \text{ K}^{-2}$ at 452 K was achieved for the composite with $x = 0.3$, which is higher than that of pure $\text{Co}_4\text{Sb}_{12}$ ($0.3 \text{ mW m}^{-1} \text{ K}^{-2}$ at 700 K) [26] and lower than that of pristine Bi_2Te_3 ($2.92 \text{ mW m}^{-1} \text{ K}^{-2}$

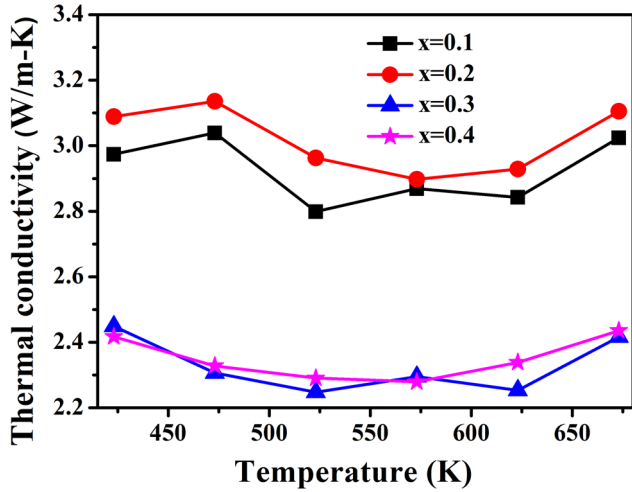


Figure 12. Temperature dependent total thermal conductivity of $(\text{Bi}_2\text{Te}_3)_x\text{Co}_4\text{Sb}_{12}$ ($x = 0.1, 0.2, 0.3, 0.4$).

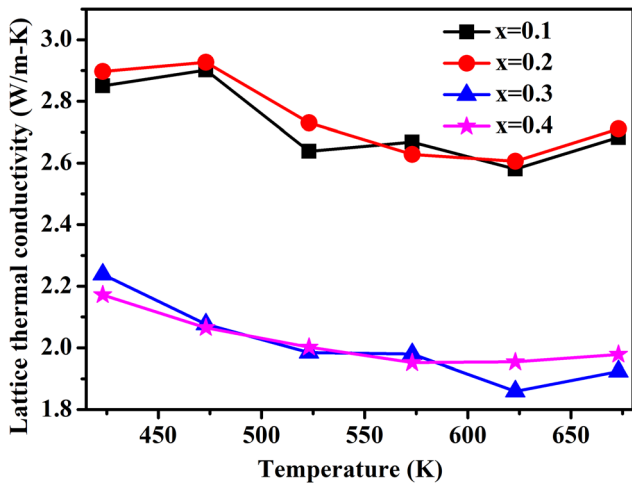


Figure 13. Temperature dependent lattice thermal conductivity of $(\text{Bi}_2\text{Te}_3)_x\text{Co}_4\text{Sb}_{12}$ ($x = 0.1, 0.2, 0.3, 0.4$).

at 300 K) [36]. The increase in power factor of the composite is due to its high electrical conductivity ($19000\text{--}35000 \text{ S m}^{-1}$ at 350 K) compared to the pristine $\text{Co}_4\text{Sb}_{12}$ (1500 S m^{-1} at 350 K) [2]. Though the Seebeck coefficient of the nanocomposite decreased slightly with increasing Bi_2Te_3 content, the very high electrical conductivity of the composite dominates over the Seebeck coefficient and increases the power factor. The power factor decreased with increasing temperature beyond 450 K. As the power factor is calculated via the relation $S^2\sigma$, the trend in the power factor with temperature for individual samples follows a similar nature like the Seebeck coefficient.

Figure 12 shows the variation in the thermal conductivity (κ) of $(\text{Bi}_2\text{Te}_3)_x\text{Co}_4\text{Sb}_{12}$ with temperature. κ is mainly composed of two parts i.e. electronic thermal conductivity (κ_e) and lattice thermal conductivity (κ_l). κ_e was calculated using the Wiedemann–Franz relation: $\kappa_e = L\sigma T$ where L is the Lorenz number, σ is the electrical conductivity of the composite and T is the temperature. κ_l was determined by subtracting κ_e from the total thermal conductivity ($\kappa_l = \kappa - \kappa_e$) and is displayed in figure 13. κ decreased first with increasing

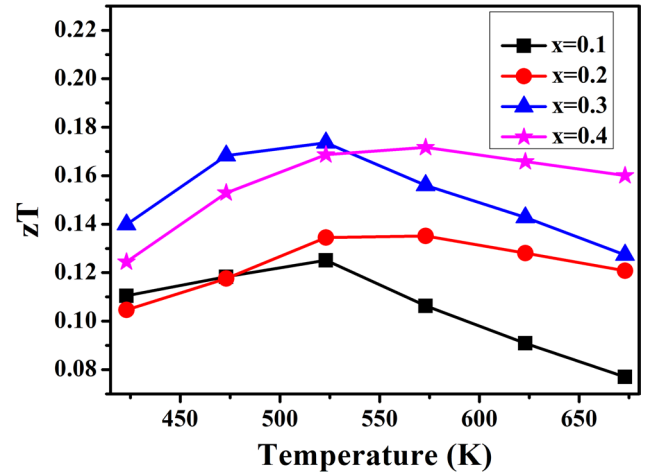


Figure 14. Temperature dependent thermoelectric figure of merit (zT) of $(\text{Bi}_2\text{Te}_3)_x\text{Co}_4\text{Sb}_{12}$ ($x = 0.1, 0.2, 0.3, 0.4$).

temperature and then increased after a certain temperature; it obeyed the $1/T$ law at lower temperatures (423–573 K) indicating that Umklapp scattering is the dominant scattering process. Bipolar conduction is responsible for the enhancement of κ at higher temperatures. The bipolar thermal conductivity is mainly generated from the diffusion of both electrons and holes and can be expressed as [44, 45]:

$$\kappa_b = \frac{\sigma_n \sigma_p}{\sigma_n + \sigma_p} (S_n - S_p)^2 T \quad (2)$$

where the subscripts n and p stand for electrons and holes respectively. This extra term in the case of bipolar conduction enhanced κ at higher temperatures. The total thermal conductivity of the composites decreased compared to bulk $\text{Co}_4\text{Sb}_{12}$ although κ_e had a higher value due to a high carrier concentration. This can be attributed to the decrease in κ_l with increasing Bi_2Te_3 content. The addition of Bi_2Te_3 nanoparticles in the sample produced many grain boundaries and interfaces. Therefore, the decrease in κ_l is due to the combined effect of (1) small-sized inclusions as confirmed by TEM and (2) increased scattering of mid-long wavelength phonons (10–100 nm) at grain boundaries and interfaces because of the incorporation of nano dispersions. Hence the Bi_2Te_3 dispersion can reduce κ without affecting σ , that is, it can decouple the interrelated σ and κ . κ of the composites decreased with increasing Bi_2Te_3 content. But in the composite with $x = 0.2$, κ was a little higher than $x = 0.1$, though κ_l was almost identical for the two samples. Identical κ_l may be due to the low concentration of Bi_2Te_3 in both the composites, which could not induce sufficient interfaces to the system to scatter phonons effectively. The larger value of κ in the composite with $x = 0.2$ occurs because of higher κ_e due to its high electrical conductivity. For composites with $x = 0.3$ and 0.4 , κ_l decreased significantly compared to $x = 0.1$ and 0.2 resulting in a very low total thermal conductivity despite of their high κ_e , probably due to the increased phonon scattering at the interfaces.

The temperature dependence of zT of the composite is shown in figure 14. The zT of the composite increased compared to pristine $\text{Co}_4\text{Sb}_{12}$. This increase can be attributed to the increased electrical conductivity and reduced thermal

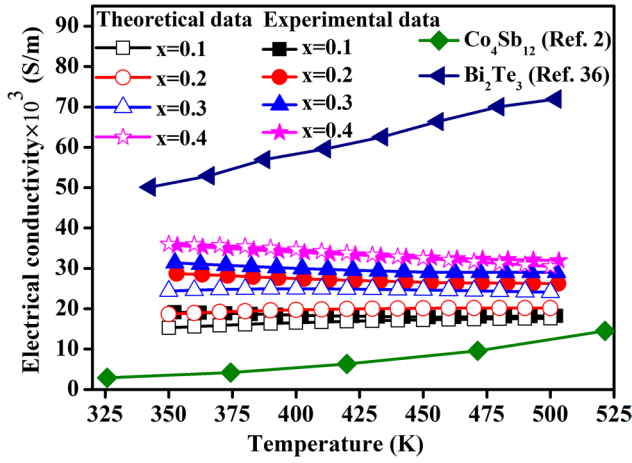


Figure 15. Comparisons between predicted and experimental electrical conductivity of $(\text{Bi}_2\text{Te}_3)_x\text{Co}_4\text{Sb}_{12}$ composites.

conductivity. The value of zT decreased with increasing temperature beyond 550 K because S decreased and κ increased in this temperature regime due to bipolar conduction. A maximum zT value of 0.17 was obtained for $(\text{Bi}_2\text{Te}_3)_{0.3}\text{Co}_4\text{Sb}_{12}$ at 523 K which is three times higher compared to $\text{Co}_4\text{Sb}_{12}$ [2]. Although the obtained zT value is relatively low compared to other reports on composite materials, the average zT improved throughout the working temperature range of 350–673 K. So, this property of maintaining the same zT over a broad temperature range is quite useful for the improvement of device performance. The average zT value was 0.15 in the temperature range between 350–673 K for $(\text{Bi}_2\text{Te}_3)_{0.3}\text{Co}_4\text{Sb}_{12}$.

4. Theoretical calculations

4.1. Theoretical predictions of electrical conductivity and thermal conductivity

The experimental results were compared with predicted transport properties by using the effective medium theories proposed by Lewis and Nielson [20, 46, 47]. Averaging or combining the properties of individual phases can predict the transport properties of composite materials. According to Lewis and Nielson, the effective electrical conductivity (σ_c) of a composite system is given by:

$$\sigma_c = \frac{1 + A \left(\frac{\sigma_s - 1}{\frac{\sigma_s}{\sigma_m} + A} \right) \phi}{1 - \phi \psi \left(\frac{\sigma_s - 1}{\frac{\sigma_s}{\sigma_m} + A} \right)}. \quad (3)$$

The same expression is also applicable for thermal conductivity. Thus, the effective thermal conductivity (κ_c) of a composite is given by:

$$\kappa_c = \frac{1 + A \left(\frac{\kappa_s - 1}{\frac{\kappa_s}{\kappa_m} + A} \right) \phi}{1 - \left(\frac{\kappa_s - 1}{\frac{\kappa_s}{\kappa_m} + A} \right) \psi \phi}, \quad (4)$$

where σ_s and σ_m are the electrical conductivities, κ_s and κ_m are the thermal conductivities of the secondary phase and matrix phase respectively, ϕ is the volume fraction of the

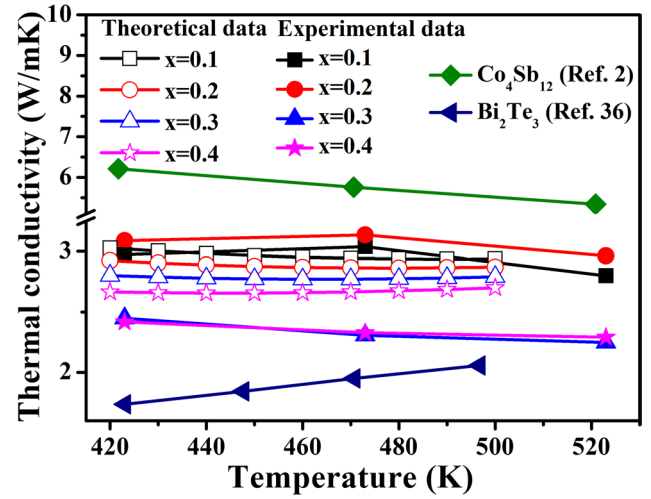


Figure 16. Measured and predicted effective thermal conductivity of $(\text{Bi}_2\text{Te}_3)_x\text{Co}_4\text{Sb}_{12}$ composites.

secondary phase, A is the shape coefficient of nanoparticles and ψ depends on the maximum packing volume fraction of nanoparticles (ϕ_m) through the equation:

$$\psi = 1 + \left(\frac{1 - \phi_m}{\phi_m^2} \right) \phi. \quad (5)$$

The Lewis–Nielson model gives the correct behaviour when $\phi \rightarrow \phi_m$ and $\frac{\sigma_s}{\sigma_m} \rightarrow \infty$.

The calculations for the transport property were performed, considering different values of ϕ_m . The best fit was obtained for $\phi_m = 0.25$. The assumption of irregularly shaped inclusions is considered in this calculation. According to Nielson [48], the value of A is 3 for irregularly shaped nanoparticles. Since Bi_2Te_3 is not stable above 500 K, its transport properties are not available above this temperature. Therefore, this model can predict properties up to 500 K. For $(\text{Bi}_2\text{Te}_3)_x\text{Co}_4\text{Sb}_{12}$ (where $x = 0.1, 0.2, 0.3, 0.4$), the corresponding volume fractions of Bi_2Te_3 are 4.43%, 8.49%, 12.22% and 15.65% respectively.

Figure 15 shows the variation in electrical conductivity with temperature as predicted from the Lewis–Nielson model using equation (3). The calculated data matched well with the experimental results, but did not follow the same temperature dependence. The measured electrical conductivity decreased with increasing temperature within 500 K because of the very high carrier concentration of the composites. The calculated data showed an increase with temperature because they followed the trend of $\text{Co}_4\text{Sb}_{12}$.

The thermal conductivity was calculated using equation (4) and plotted with respect to temperature in figure 16. The calculated effective thermal conductivity of the composites systematically decreased with the addition of Bi_2Te_3 content following the behaviour of $\text{Co}_4\text{Sb}_{12}$. For composites with $x = 0.3$ and 0.4 , the calculated κ did not match the experimental data. Since the Lewis–Nielson method does not consider the effect of interfaces and grain boundaries, this can be attributed to the increased phonon scattering at matrix–nanoparticle interfaces for higher concentrations of the Bi_2Te_3 . Therefore it is very difficult to theoretically predict

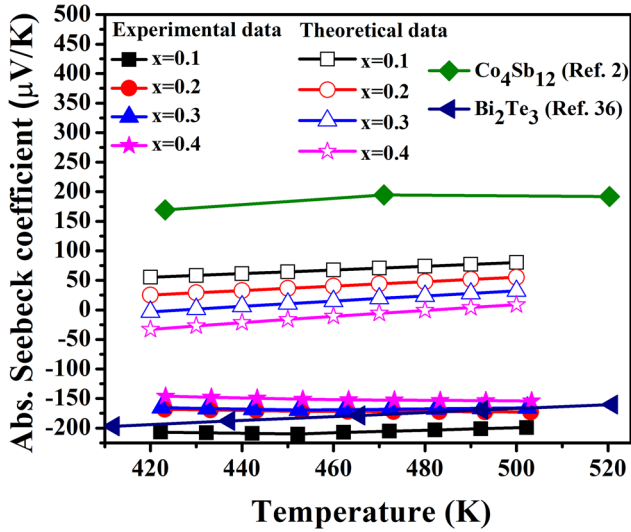


Figure 17. Calculated effective Seebeck coefficient of $(\text{Bi}_2\text{Te}_3)_x\text{Co}_4\text{Sb}_{12}$ composites compared with the experimental data.

the thermal conductivity of composites without considering interface scattering.

4.2. Theoretical prediction of Seebeck coefficient

Following the strategy of effective medium theory, Webman *et al* [36, 49] derived a formula for the Seebeck coefficient that depends on both the electrical conductivity and thermal conductivity of the individual phases present in the composite material and is given by:

$$\phi_m \frac{\sigma_m(S_c - S_m)}{(2\sigma_c + \sigma_m)(2\kappa_c + \kappa_m)} + \phi_s \frac{\sigma_s(S_c - S_s)}{(2\sigma_c + \sigma_s)(2\kappa_c + \kappa_s)} = 0, \quad (6)$$

where S is the Seebeck coefficient, κ is the thermal conductivity, σ is the electrical conductivity and the subscripts m , s and c denote the matrix phase, secondary phase and composite medium respectively. The WJC model is more accurate in the case of a high $\frac{\sigma_s}{\sigma_m}$ ratio.

The effective Seebeck coefficients for nanocomposites were calculated using equation (6) and are shown in figure 17. The measured data are different from the calculated Seebeck coefficient in contrast to the electrical and thermal conductivities. The calculated Seebeck coefficient was positive whereas the measured Seebeck coefficient was negative. The WJC model failed to calculate S correctly because S_m and S_s have different signs. The chemical potential (μ) of the two phases are different in a composite. This difference is large when one phase is p type and another phase is n type. As charge carriers transfer from one phase to the other, an additional contribution (function of μ) will feature in the calculation of the Seebeck coefficient [50–52]:

$$\Delta S = \frac{1}{|e|} \frac{d\mu}{dT} \quad (7)$$

where T is the temperature and e is the unit charge. When S_m and S_s have the same sign, this extra contribution is very

small and can be neglected. With different signs of S_m and S_s , it is not negligible. Webman *et al* had not considered this extra term in their equation.

The overall effect of nano-inclusions on the thermoelectric properties of composites depends on many factors such as the concentration of nanoparticles in the matrix and the potential barrier, position of Fermi level and boundary between the two phases. The exact calculation of transport properties is not possible. The theories can only develop a reasonable approximation of transport properties considering the properties and relative fractions of the components.

5. Conclusions

$(\text{Bi}_2\text{Te}_3)_x\text{Co}_4\text{Sb}_{12}$ (where $x = 0.1, 0.2, 0.3, 0.4$) composite thermoelectric materials were fabricated by high energy ball-milling followed by spark plasma sintering. The influence of dispersions on the thermoelectric properties of composites was investigated in the temperature range of 350–673 K. Structural and morphological studies were carried out using SEM, EPMA, EBSD and TEM. The Rietveld analysis of XRD patterns showed that Bi_2Te_3 is present in the composites as a secondary phase. The SEM micrographs also supported the XRD analysis. The presence of a small amount of Sb was observed in the samples for $x \geq 0.2$ in EPMA. The EBSD analysis showed that the average grain size of $\text{Co}_4\text{Sb}_{12}$ in composites was 1 μm . Bi_2Te_3 inclusions were agglomerated in the grain boundary and dispersed randomly throughout the bulk matrix $\text{Co}_4\text{Sb}_{12}$, which affected the thermoelectric properties significantly. The electrical conductivity increased and the Seebeck coefficient of the composites reduced on the addition of Bi_2Te_3 due to the increased carrier concentration. The composites showed n-type conduction whereas the majority of charge carriers in the case of $\text{Co}_4\text{Sb}_{12}$ were holes. The overall power factor of composites improved compared to pristine $\text{Co}_4\text{Sb}_{12}$ due to the high electrical conductivity. A decrease in the thermal conductivity was observed, which could be attributed to the enhancement of phonon scattering at interfaces caused by the dispersed Bi_2Te_3 in the $\text{Co}_4\text{Sb}_{12}$ matrix. The enhanced zT of composites over a broad temperature range (350–673 K) was due to their higher electrical conductivity and lower thermal conductivity. A maximum zT of 0.17 was achieved for $(\text{Bi}_2\text{Te}_3)_{0.3}\text{Co}_4\text{Sb}_{12}$ at 523 K and the average zT value was 0.15 from 350 K to 673 K. Though the obtained zT is not as high as in previous reports, this composite approach is a very effective way to produce high performance thermoelectric materials. Optimization of inclusion size, proper composition and homogeneous distribution of Bi_2Te_3 in $\text{Co}_4\text{Sb}_{12}$ matrix can help to achieve higher zT . Therefore, this approach can be applied to high zT thermoelectric materials such as doped or filled $\text{Co}_4\text{Sb}_{12}$ for further improvement in zT .

Acknowledgments

This work was supported by the Department of Science and Technology (DST), India, grant number SB/EMEQ-243/2013.

ORCID iDs

Ramesh Chandra Mallik  <https://orcid.org/0000-0002-8383-7812>

References

- [1] Zhao L D, Lo S H, Zhang Y, Sun H, Tan G, Uher C, Wolverton C, Dravid V P and Kanatzidis M G 2014 *Nature* **508** 373–7
- [2] Itoh T, Hattori E and Kitagawa K 2008 *J. Propul. Power* **24** 359–64
- [3] Wu T, Bai S Q, Shi X and Chen L D 2013 *J. Inorg. Mater.* **28** 224–8
- [4] Rogl G, Grytsiv A, Koblyuk N M, Bauer E, Laumann S and Rogl P 2011 *J. Phys.: Condens. Matter* **23** 275601
- [5] Tang Y, Hanus R, Chen S W and Snyder G J 2015 *Nat. Commun.* **6** 7584
- [6] Tang Y, Qiu Y, Xi L, Shi X, Zhang W, Chen L, Tseng S M, Chen S and Snyder G J 2014 *Energy Environ. Sci.* **7** 812–9
- [7] Mallik R C, Jung J Y, Ur S C and Kim I H 2008 *Met. Mater. Int.* **14** 223–8
- [8] Su X, Li H, Yan Y, Wang G, Chi H, Zhou X, Tang X, Zhang Q and Uher C 2012 *Acta Mater.* **60** 3536–44
- [9] Mallik R C, Anbalagan R, Rogl G, Royanian E, Heinrich P, Bauer E, Rogl P and Suwas S 2013 *Acta Mater.* **61** 6698–711
- [10] Liang T, Su X, Yan Y, Zheng G, Zhang Q, Chi H, Tang X and Uher C 2014 *J. Mater. Chem. A* **2** 17914–18
- [11] Duan B et al 2016 *Energy Environ. Sci.* **9** 2090–8
- [12] Mallik R C, Anbalagan R, Raut K K, Bali A, Royanian E, Bauer E, Rogl G and Rogl P 2013 *J. Phys.: Condens. Matter* **25** 105701–10
- [13] David S M, Blaszkiewicz M and Newnham R E 1990 *J. Am. Ceram. Soc.* **73** 2187–203
- [14] Wang M and Pan N 2008 *Mater. Sci. Eng. R* **63** 1–30
- [15] Nishio Y and Hirano T 1997 *Japan. J. Appl. Phys.* **36** 170–4
- [16] Popescu A, Woods L M, Martin J and Nolas G S 2009 *Phys. Rev. B* **79** 205302
- [17] Moyzhes B and Nemchinsky V 1998 *Appl. Phys. Lett.* **73** 1895–7
- [18] Bergman D J and Fel L G 1999 *J. Appl. Phys.* **85** 8205–16
- [19] Bergman D J and Levy O 1991 *J. Appl. Phys.* **70** 6821–33
- [20] Pietrak K and Winiewski T S 2015 *J. Power Technol.* **95** 14–24
- [21] Landauer R 1952 *J. Appl. Phys.* **23** 779–84
- [22] Brochin F, Lenoir B, Devaux X, Lopez R M and Scherrer H 2000 *J. Appl. Phys.* **88** 3269–75
- [23] Shi X, Chen L D, Bai S Q, Huang X Y, Zhao X Y, Yao Q and Uher C 2007 *J. Appl. Phys.* **102** 103709
- [24] Zhou X, Wang G, Zhang L, Chi H, Su X, Sakamoto J and Uher C 2012 *J. Mater. Chem.* **22** 2958–64
- [25] He Z, Stiewe C, Platzek D, Karpinski G, Müller E, Li S, Toprak M and Muhammed M 2007 *Nanotechnology* **18** 235602
- [26] Feng B, Xie J, Cao G, Zhu T and Zhao X 2013 *J. Mater. Chem. A* **1** 13111–9
- [27] Zhao D, Zuo M, Leng J and Geng H 2013 *Intermetallics* **40** 71–5
- [28] Chubilleau C, Lenoir B, Masschelein P, Dauscher A, Candolfi C, Guilmeau E and Godart C 2013 *J. Mater. Sci.* **48** 2761–6
- [29] Zhu Y, Shen H and Chen H 2012 *Rare Met.* **31** 43–7
- [30] Gharleghi A, Liu Y, Zhou M, He J, Tritt M T and Liu C J 2016 *J. Mater. Chem. A* **4** 13874–80
- [31] Zhao X Y, Shi X, Chen L D, Zhang W Q, Bai S Q, Pei Y Z, Li X Y and Goto T 2006 *Appl. Phys. Lett.* **89** 92121
- [32] Rogl G, Grytsiv A, Rogl P, Peranio N, Bauer E, Zehetbauer M and Eibl O 2014 *Acta Mater.* **63** 30–43
- [33] Xiong Z, Chen X, Huang X, Bai S and Chen L 2010 *Acta Mater.* **58** 3995–4002
- [34] Moure A, Bravo M R, Abad B, Campo A D, Rojo M M, Aguirre M H, Jacquot A, Fernandez J F and Gonzalez M M 2017 *Nano Energy* **31** 393–402
- [35] Rogl G, Grytsiv A, Failamani F, Hochenhofer M, Bauer E and Rogl P 2017 *J. Alloys Compd.* **695** 682–96
- [36] Liu W, Lukas K C, McEnaney K, Lee S, Zhang Q, Opeil C P, Chen G and Ren Z 2013 *Energy Environ. Sci.* **6** 552–60
- [37] Webman I, Jortner J and Cohen M H 1977 *Phys. Rev. B* **16** 2959–64
- [38] Chen X, Liu L, Dong Y, Wang L, Chen L and Jiang W 2012 *Prog. Nat. Sci. Mater. Int.* **22** 201–6
- [39] Ioffe A F, Stil'bans L S, Iordanishvili E K and Stavitskaya T S 1957 *Semiconductor Thermoelements and Thermoelectric Cooling* (London: Infosearch)
- [40] Gibbs Z M, Kim H S, Wang H and Snyder G J 2015 *Appl. Phys. Lett.* **106** 022112
- [41] Rowe D M and Bhandari C M 1983 *Modern Thermoelectrics* (London: Holt, Rinehart and Winston)
- [42] Sofu J O and Mahan G D 1998 *Phys. Rev. B* **58** 15620–3
- [43] Goldsmid H J 1958 *Proc. Phys. Soc.* **71** 633
- [44] Price P J 1955 *London Edinburgh Dublin Phil. Mag. J. Sci.* **46** 1252–60
- [45] Drabble J R and Goldsmid H J 1961 *Thermal Conduction in Semiconductors* (New York: Pergamon)
- [46] Progelhof R C, Throne J L and Ruetsch R R 1976 *Polym. Eng. Sci.* **16** 615–25
- [47] Pal R 2008 *Composites A* **39** 718–26
- [48] Nielsen L E 1973 *J. Appl. Polym. Sci.* **17** 3819–20
- [49] Vaney J B et al 2015 *J. Mater. Chem. C* **3** 11090–8
- [50] Sonntag J 2009 *J. Phys.: Condens. Matter* **21** 175703
- [51] Sonntag J 2006 *Phys. Rev. B* **73** 045126
- [52] Sonntag J 2016 *J. Mater. Chem. C* **4** 10973–6